Available online at www.sciencedirect.com

ScienceDirect

Procedia Structural Integrity 76 (2026) 59–66

Structural Integrity Procedia

www.elsevier.com/locate/procedia

5th International Symposium on Fatigue Design and Material Defects FDMD 2025

Threshold and propagation of defects under RCF: an experimental approach

N. Zani[a], P. M. Rao[b], S. Foletti[b], J. Y. Buffiere[c], A. Mazzu'[a], S. Beretta[b,d,*]

[a]*Universita' degli Studi di Brescia, Department of Industrial and Mechanical Engineering, Via Branze 38, 25123 Brescia, Italy*
[b]*Politecnico di Milano, Department of Mechanical Engineering, via La Masa 1, 20156 Milano, Italy*
[c]*INSA Lyon, MATEIS, CNRS, 9 Av. Jean Capelle O, 69100 Villeurbanne, France*
[d]*Auburn University, National Center for Additive Manufacturing Excellence (NCAME), Auburn, Al 36849*

Abstract

This study investigates the threshold and propagation behavior of artificial defects under rolling contact fatigue (RCF) through a combined experimental methodology. Multiaxial fatigue tests on gear steel specimens with ring-shaped EDM defects were used to evaluate Mode II and Mode III thresholds under out-of-phase axial-torsional loading. Complementary bidisc tests on crowned specimens assessed crack growth under lubricated conditions at varying Hertzian pressures. Crack propagation was monitored via high-resolution tomography and quantified using finite element models to compute stress intensity factors. Coplanar shear-driven growth was observed in both setups, with Mode II as the dominant mechanism. A predictive methodology integrating experimental crack growth data and numerical modeling showed strong agreement with fatigue lives, underscoring the relevance of combining multiaxial and RCF approaches in defect tolerance analysis.

Keywords: Multiaxial fatigue; Rolling contact fatigue; Defect; threshold; life assessment.

1. Introduction

Modern high-power mechanical transmissions, such as those in aerospace propulsion systems, increasingly employ planetary gears with integrated bearings to meet stringent efficiency and packaging demands. These components operate under severe rolling contact fatigue (RCF), characterized by multiaxial, non-proportional stresses and high contact pressures. A typical failure mode involves subsurface crack initiation from small surface or near-surface defects, with propagation mainly driven by shear stresses Donzella et al. (2011), Rejith et al. (2023).

Traditional stress-based fatigue criteria tend to underestimate the failure risk in shear-dominated regimes. For this reason, a damage tolerance approach—based on mixed-mode crack growth, with particular attention to Modes II and

* Corresponding author
E-mail address: stefano.beretta@polimi.it

2452-3216
10.1016/j.prostr.2025.12.287

III—offers a more appropriate framework Rao et al. (2022); Foletti et al. (2014). However, experimental data in these conditions are still scarce, mainly due to the challenges in reproducing controlled crack propagation driven by out-of-phase shear loading.

Improving fatigue life prediction requires identifying threshold and growth behavior under realistic RCF. Donzella et al. (2011, 2013) proposed failure assessment methods based on defect-driven propagation and stress intensity thresholds. Kunzelmann et al. (2023) applied linear elastic fracture mechanics to model crack growth in bearing steels using experimental data. Ren et al. (2022) further emphasized the relevance of Mode III effects in 3D crack fronts, underlining the need for models that capture realistic loading paths and crack evolution in advanced components.

This work presents an integrated experimental methodology to assess crack threshold and propagation under RCF. It combines multiaxial fatigue and lubricated bidisc tests on samples with artificial defects, targeting shear-driven crack growth (Modes II and III). The results support the development of predictive models and empirical growth laws for reliable life estimation of critical mechanical components.

Nomenclature

c	Paris law coefficient
E	Young's modulus
f_{II}	Geometric correction factor for Mode II
f_{III}	Geometric correction factor for Mode III
FPB	Filtered back-projection (reconstruction algorithm)
m'	Paris law exponent
p	Hertzian contact pressure
$p_{\min}$	Minimum applied contact pressure
SIF	Stress Intensity Factor
$\Delta K_{I,th,LC}$	Threshold SIF for long cracks in Mode I
ΔK_{II}	Mode II stress intensity factor range
$\Delta K_{II,th}$	Threshold SIF for Mode II
ΔK_{III}	Mode III stress intensity factor range
$\Delta K_{III,th}$	Threshold SIF for Mode III
$\Delta\sigma$	Normal stress range
$\Delta\tau$	Shear stress range
ν	Poisson's ratio

2. Materials and Methods

2.1. Multiaxial tests

The multiaxial test was performed using the MTS Series 809 Axial/Torsional Test System on round specimens made of a gear steel. The specimens included artificial ring-shaped defects, introduced by electro-discharge machining (EDM), with a radius of 200 μm (Figure 1a). An initial uniaxial pre-cracking phase, consisting of 10^7 cycles under a high negative load ratio, was employed to promote the activation of favorable crack planes. Upon SEM confirmation of pre-crack formation, the main loading phase with combined axial-torsional stresses was then carried out following the procedure described by Foletti et al. (2014). The loading path ratio between shear stress ($\Delta\tau$) and normal compressive stress ($\Delta\sigma$) was set to 1.8, with stresses applied out of phase (90°) to simulate the actual stress state under rolling contact conditions (Figure 1b).

The Mode II and Mode III stress intensity factors (SIF) were calculated using elliptical crack shape functions from Kassir and Sih (1966):

$$\Delta K_{III} = f_{III} \cdot \Delta\tau \cdot \sqrt{\pi a} \tag{1}$$

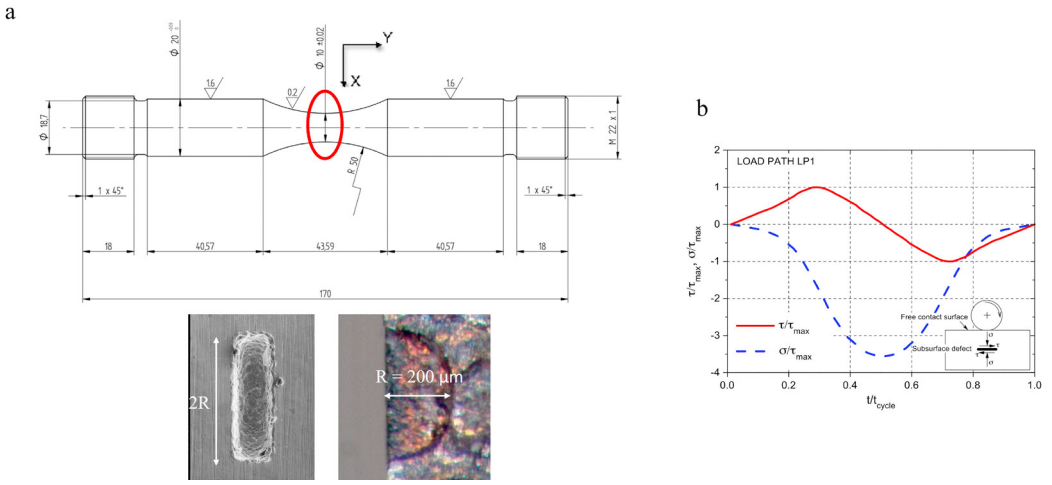

Fig. 1. (a) Shape and size of the multiaxial sample; (b) Load path for multiaxial samples.

$$\Delta K_{III} = f_{III} \cdot \Delta\tau \cdot \sqrt{\pi a} \tag{2}$$

where $f_{III} = 0.5243$, $f_{II} = 0.7490$ and a = total crack radius (defect + pre-crack).

The thresholds $\Delta K_{III,th}$ and $\Delta K_{II,th}$ were determined by gradually reducing applied stresses until no crack propagation was observed over 5×10^6 cycles. After testing, specimens were heat-tinted to highlight propagation surfaces and then fractured under fatigue for further fractographic analysis.

2.2. *Rolling contact fatigue tests*

Rolling contact tests were carried out by means of the bidisc test bench described elsewhere (Donzella et al. (2011)). Six crowned disc specimens were machined out from a bar in gear steel. Two artificial holes with diameter of 0.4 mm and depth of 0.27 mm were machined by EDM in each of six specimens (Figure 2); the counteracting sample, also manufactured in gear steel, was surface hardened and left without defects, to prevent fatigue failure during the tests.

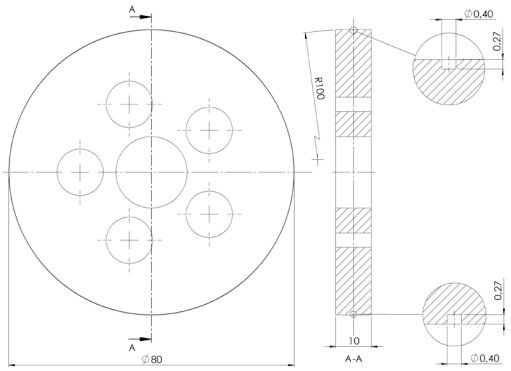

Fig. 2. Schematic of the disc-shaped specimen

In all the tests the contact was lubricated by a jet of MOBILGEAR 600 XP 150 oil. The rolling speed was 900 r.p.m. for both specimens. The applied load varied in each test, such to build a S-N curve. The maximum duration of the tests was fixed to 2×10^7 cycles, unless earlier failure occurred.

Laboratory tomography (Phoenix-xray, MATEIS) was used to observe crack propagation in the discs. Due to high X-ray absorption, full discs (Figure 3a) were machined into smaller specimens (4.5×1×18 mm; Figure 3b) for Lab

CT scanning at 160 kV, 2 µm voxel size, 667 ms exposure, 1200 projections 3D images were reconstructed via FBP. Sub-surface cracks from surface defects (Figure 3d) had low contrast, so a Hessian matrix-based method (Xiao and Buffiere (2021)) was used to extract planar features and segment cracks (Figures 3e–f). For rolling contact fatigue crack propagation analysis, it is important to quantify the crack propagation length along the rolling direction versus transverse on the rolling direction. The propagation lengths of the crack in the above two directions are defined as the projected distances between the two opposite crack tips subtracted by the diameter of the hole bottom (d = 0.36 mm) within central tomography slices. For example, as shown in Figure 3, the crack propagation length transverse is detected as ($L - d$).

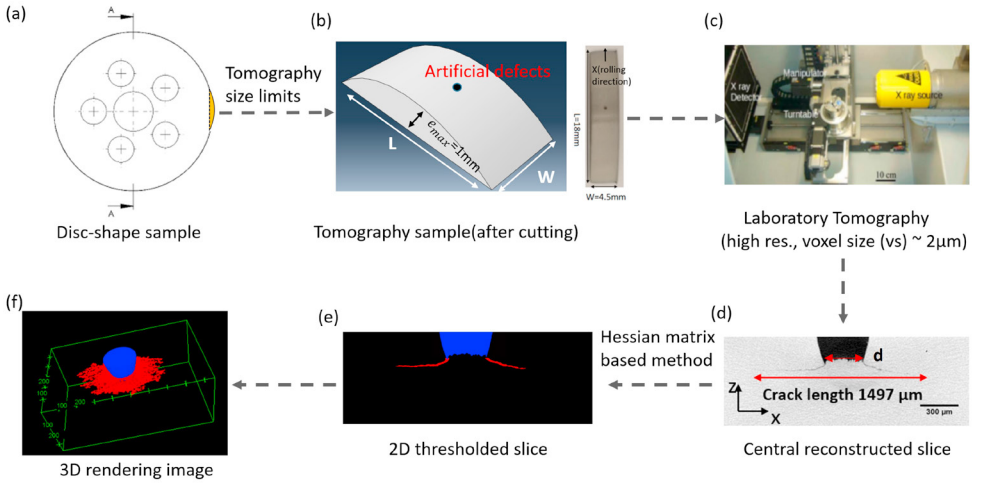

Fig. 3. Schematic of the process of 3D characterization of cracks within disc-shape specimens (a) Geometry of disc-shape specimens; (b) The cut sample to meet the requirements of high resolution and X-ray penetration in tomography; (c) Laboratory tomography scans (voxel size about 2 μm;(d) Reconstructed slice (along the rolling direction); (e) Crack segmentation image by Hessian Matrix based method Xiao and Buffiere (2021) (f) 3d rendering of crack image.

The stress intensity factor ranges of cracks nucleated at the edge-bottom for bidisc samples were estimated using finite element (FE) models developed in ABAQUS®. Figure 4 shows the flat plate model representing the bearing, where a half-symmetric, linear-elastic setup was used (E = 210 GPa, ν = 0.3). The bottom surface was clamped, and the rolling contact was simulated via a moving Hertzian load passing over the defect in 24 time-steps, covering a total distance of 5 mm to replicate one complete load cycle. A general contact interaction with a friction coefficient of 0.6 was applied on the crack surfaces. The crack was modeled as a ring at the bottom hole edge, with a radius ranging from 0.180 to 0.700 mm, and was finely meshed (0.002 mm) near the tip to ensure convergence. Mode II (rolling direction) and Mode III (transverse direction) ΔK were calculated from the quarter-node displacements using Williams' equations (Kuna (2013)):

$$K_{II} = (u_1 - u_2) \cdot \frac{E\sqrt{\frac{2\pi}{r}}}{8(1-\nu^2)} \tag{3}$$

$$K_{III} = (w_1 - w_2) \cdot \frac{E\sqrt{\frac{\pi}{2r}}}{4(1+\nu)} \tag{4}$$

where u_1, u_2, w_1 and w_2 are the crack shear displacements (CSD) at the tip and r is the distance of the quarter nodes from the crack tip. Figure 5 shows the dimensionless SIF range $\Delta K_{II}/\Delta K_{I,th}$ and $\Delta K_{III}/\Delta K_{I,th}$ as a function of the crack radius under various contact pressures.

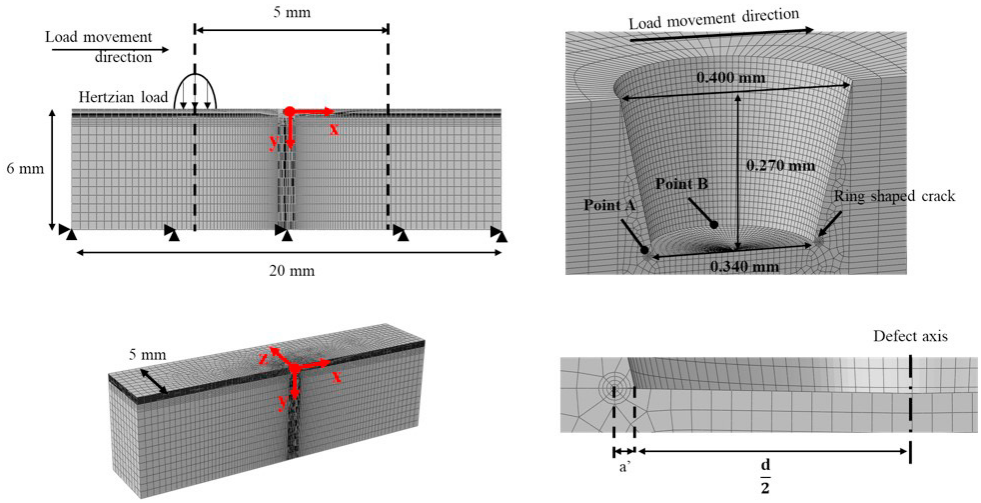

Fig. 4. Finite element model of the sample with the artificial defect.

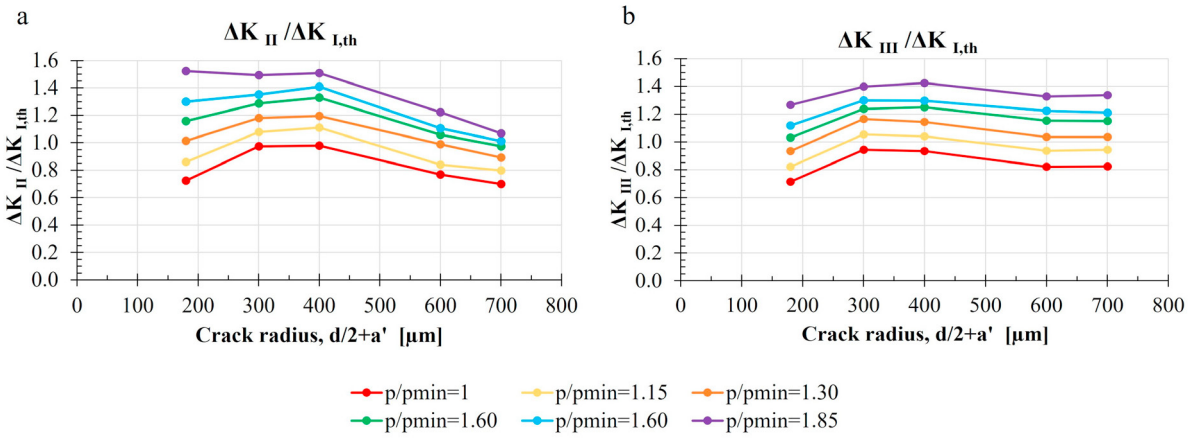

Fig. 5. Stress intensity factor range as a function of crack size under various contact pressures.

3. Results and discussion

The crack propagation behavior under multiaxial out-of-phase loading is governed by coplanar shear mechanisms, with pure Mode II propagation occurring along the crack plane (Figure 6a) and Mode III deformation localized at the defect tip (Figure 6b), consistently with the observations reported in Foletti et al. (2014). Quantitative analysis indicates that Mode II propagation dominates over Mode III (Figure 6c). The relationship between the coplanar crack growth rate, $\Delta a/\Delta N$, and the applied stress intensity factor range, normalized by the long-crack Mode I threshold $\Delta K_{I,th,LC}$, is illustrated in Figure 7. For the multiaxial specimens, the normalized threshold values were determined as $\Delta K_{III}/\Delta K_{I,th,LC} = 0.52$ for Mode III and $\Delta K_{II}/\Delta K_{I,th,LC} = 0.74$ for Mode II, highlighting the more significant contribution of in-plane shear to the overall crack advance.

The results of the bidisc tests are summarized in Figure 8, showing test duration on the abscissa and normalized Hertzian pressure, p/p_{min}, on the ordinate. Cracks detected in the transverse direction by tomography are shown next to each point. Tests with p/p_{min} between 1.30 and 1.85 revealed spall formation at one artificial defect per specimen, with spall width comparable to the contact patch. In accordance with the findings of Hashimoto et al. (2019) and Ren et al. (2022), an elliptical, transversely elongated region appeared around the defect base, indicating initial transverse propagation followed by rolling-direction growth. Transverse growth likely ceased upon reaching low-stress zones,

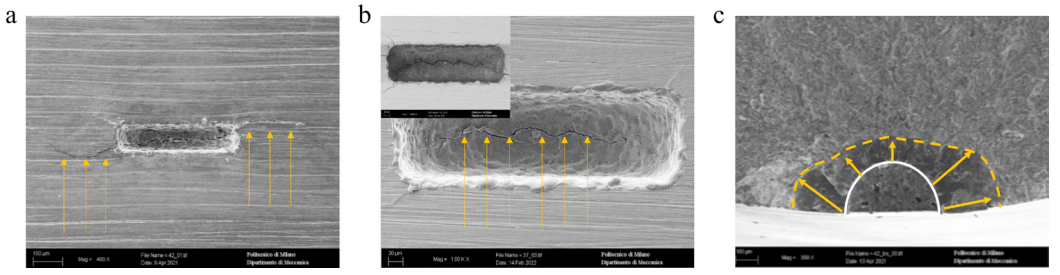

Fig. 6. Coplanar propagation cracks under out-of-phase fatigue tests.

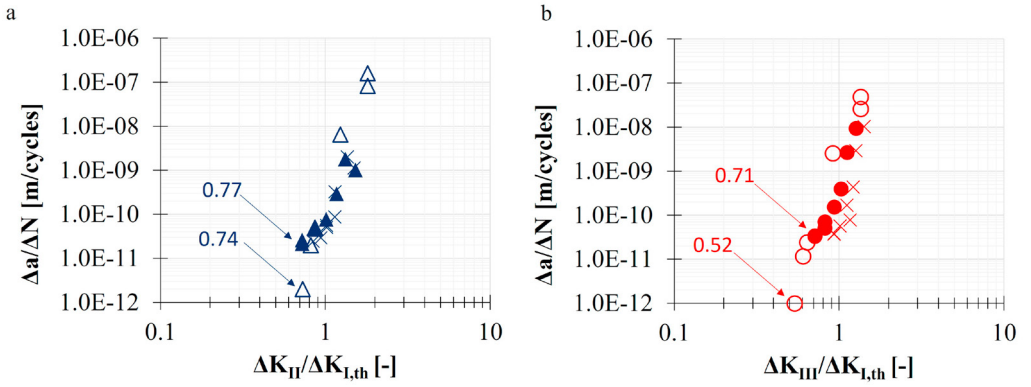

Fig. 7. Coplanar crack growth rate versus normalised strees intensity factor range in mode II (a) and mode III (b) according to multiaxial tests (empty icons), rolling contact tests when SIF range at initiation is considered (full icons) and rolling contact contact tests when SIF range at the end of the test is considered (cross icons).

while cyclic rolling-direction stresses promoted further advance. Cracks consistently nucleated at the defect base and propagated coplanarly, as illustrated in Figure 9 for $p/p_{min} = 1.47$, as also demonstrated by Donzella et al. (2011, 2013) and Zani et al. (2025).

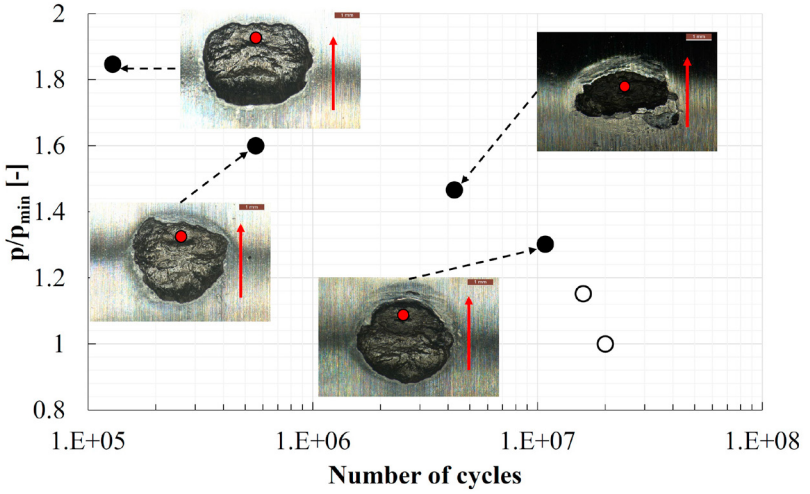

Fig. 8. The bidisc fatigue testing results of different normalized Hertz pressures and number of cycles detected by Lab-CT.

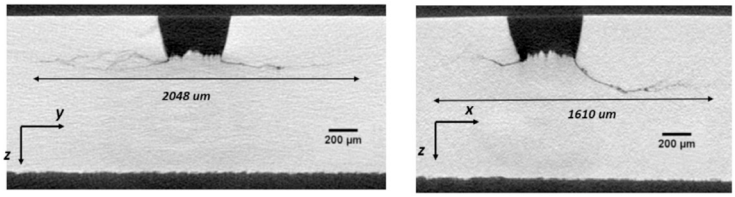

Fig. 9. Coplanar crack propagation in bidisc samples in the transverse plane (on the left) and in the rolling plane (on the right) (p/p_{min} = 1.15).

Figure 7 also reports the crack propagation rates measured in the bidisc tests as a function of the stress intensity factor (SIF) range. To account for the SIF behavior as a function of crack length, we considered both the case where ΔK corresponds to the initiation value (assuming a 10 µm crack at the base of the hole) and the case where ΔK is calculated using the crack length measured by CT scan at the end of the test. Regardless of the chosen approach, Mode II does not exhibit significant variations, whereas Mode III points shift toward slightly higher ΔK values. A comparison with the multiaxial tests reveals that the bidisc data align well with the multiaxial values in the propagation regime, suggesting that the two experimental methods are compatible in describing the crack propagation behavior. However, no clear threshold could be identified; to accurately determine it, additional tests at lower applied pressures would have been necessary.

To conclude this work, we aimed to combine the two developed approaches to build a predictive methodology capable of estimating the behavior observed in the bidisc experiments. To achieve this, we applied Paris' law using the c and m' parameters determined from the multiaxial specimens (see Table **??** for values). A crucial aspect of this combination was how ΔK was handled. On one hand, we used the FEM results with a friction coefficient of 0.6 between the crack faces, calculating ΔK step by step as a function of the evolving crack length, thus accounting for its variation during propagation. On the other hand, we adopted a simplified approach, using a constant initial value of ΔK corresponding to the onset of propagation. Figure 10a shows the results for Mode II, and Figure 10b shows those for Mode III. Specifically, for Mode II, both predictive approaches yielded results closely aligned with the experimental data: both the full FEM model (with variable ΔK) and the simplified model (with constant initial ΔK) showed good agreement, demonstrating that the methodology effectively captures the material's behavior under these conditions. For Mode III, the FEM approach with friction 0.6 maintained good consistency with the experiments at moderate contact pressures but showed some deviation at higher pressures. The simplified model, based solely on the initial ΔK, produced less conservative results, tending to underestimate the fatigue life.

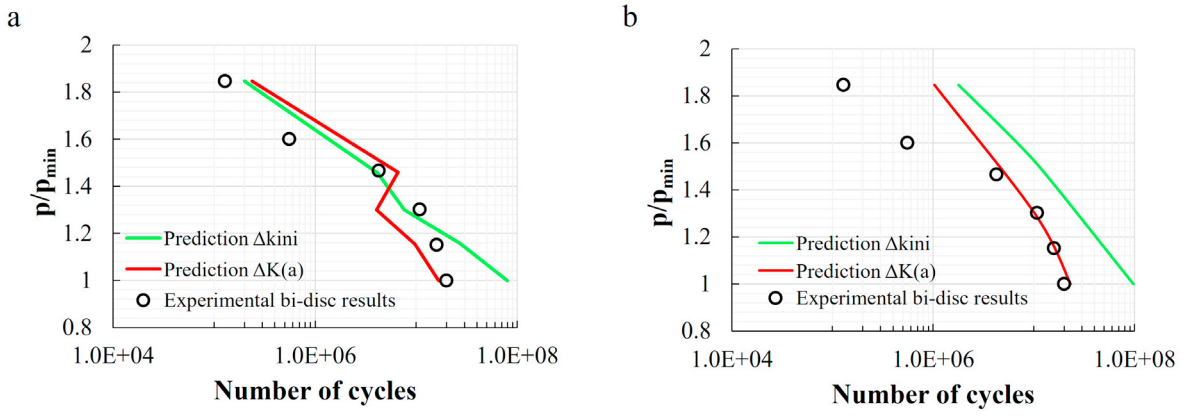

Fig. 10. Prediction model for bidisc tests: (a) Mode II; (b) Mode III.

4. Conclusions

This work combined multiaxial axial-torsional fatigue tests and bidisc RCF experiments to investigate defect threshold and propagation in gear steel. The main findings are as follows:

- Both setups consistently showed coplanar crack propagation, with in-plane shear (Mode II) as the dominant mechanism.
- Multiaxial tests yielded reliable Mode II and III thresholds and Paris' law parameters for modeling.
- Bidisc tests, though more complex in ΔK estimation, provided realistic insights into crack propagation behavior.
- The combined predictive model effectively captured fatigue lives in Mode II, while Mode III predictions were less conservative at high pressures.

These results highlight the value of integrating multiaxial and contact-based fatigue testing with numerical modeling to predict defect evolution in bearing materials.

Acknowledgment

The IDERPLANE project has received funding from the *Clean Sky 2 Joint Undertaking* under the European Union's *Horizon 2020 research and innovation program* under grant agreement No. 821315. Mr. Andrea Piazza (AvioAero, Rivalta di Torino (TO), Italy), the Topic Manager of the project, is gratefully acknowledged for his support.

References

Concli, F.; Mastrone, M.N. Advanced Lubrication Simulations of an Entire Test Rig: Optimization of the Nozzle Orientation to Maximize the Lubrication Capability. *Lubricants* **2023**, *11*(7), 300.

Donzella, G., Faccoli, M., Mazzù, A., Petrogalli, C., Desimone, H., 2011. Influence of inclusion content on rolling contact fatigue in a gear steel: Experimental analysis and predictive modelling. *Engineering Fracture Mechanics* 78, 2761–2774.

Donzella, G., Petrogalli, C., 2010. A failure assessment diagram for components subjected to rolling contact loading. *International Journal of Fatigue* 32, 1685–1695.

Donzella, G., Mazzù, A., Petrogalli, C., 2013. Failure assessment of subsurface rolling contact fatigue in surface hardened components. *Engineering Fracture Mechanics* 103, 26–38.

Hashimoto, S., Yokoi, D., Shimizu, T., 2019. Quantitative evaluation of the flaking strength of rolling bearings with small defects as a crack problem. *International Journal of Fatigue* 126, 354–365.

Foletti, S., Beretta, S., Tarantino, M.G., 2014. Multiaxial fatigue criteria versus experiments for small crack under rolling contact fatigue. *International Journal of Fatigue* 58, 181–192.

Kassir, M.K., Sih, G.C., 1966. Three-dimensional stress distribution around an elliptical crack under arbitrary loadings. *Journal of Applied Mechanics* 33(3), 601–611.

Kuna, M., 2013. Finite elements in fracture mechanics. *Solid Mechanics and Its Applications* 201. Springer.

Kunzelmann, M., Papadopoulos, I.V., Berto, F., 2023. Prediction of RCF crack propagation. *Tribology International* 181, 108345.

Rao, P.M., Foletti, S., Bonaiti, L., Concli, F., Gorla, C., Beretta, S., 2022. Mode III threshold under Rolling Contact Fatigue and development of a test gearbox for planet gears. *Forschung im Ingenieurwesen* 86, 483–490.

Rejith, R., Pillai, P., Madhavan, V., 2023. Bearings for aerospace application. *Aerospace Science and Technology* 140, 107461.

Ren, Y., Sun, Y., Zhou, Y., Zhang, J., 2022. Subsurface crack propagation under rolling contact fatigue. *Engineering Fracture Mechanics* 272, 108690.

Xiao, C., Buffiere, J.-Y., 2021. Neural network segmentation methods for fatigue crack images obtained with X-ray tomography. *Engineering Fracture Mechanics* 252, 107823.

Zani, N., Petrogalli, C., Shu, K., Cantaboni, F., Ginestra, P.S., 2025. Rolling contact fatigue perspective of damage mechanism in 3D printed 17–4 PH stainless steel. *Tribology International* 211, 110868. https://doi.org/10.1016/j.triboint.2025.110868.